Nano Research

Open Access

Research Article

Amino-functionalized and Na^+ pre-intercalated three-dimensional $Ti_3C_2T_x$ film aerogel with excellent electrochemical performances for supercapacitor

Xinhui Jin[1], Dejie Mo[1], Lirong Feng[1], Dong Wang[1], Baolian Su[2], and Xiaohui Guo[1] ✉

[1] *Key Lab of Synthetic and Natural Functional Molecule Chemistry of Ministry of Education, The College of Chemistry and Materials Science, Northwest University, Xi'an 710069, China*
[2] *Department of inorganic chemistry, University of Namur, 61 rue de Bruxelles, B-5000 Namur, Belgium*

Cite this article: *Nano Research*, **2025**, *18*, 94907092. https://doi.org/10.26599/NR.2025.94907092

ABSTRACT: Precise modulation of the pore structure and modification of the surface groups (–NH_2) of MXene aerogels by the solid foaming method in combination with Na^+ pre-intercalation can significantly increase the layer spacing and change the electronic structure of MXene, thereby significantly optimizing its electrochemical performance. The three-dimensional (3D) network structure provides numerous active sites on the surface of MXene and provides more ion transfer pathways and the large layer spacing allows electrolyte ions fast transport and the surface groups provide more active sites for the pseudocapacitive reaction. As a result, the prepared Na-$Ti_3C_2T_x$ (where T is –O, –OH, –F, and/or –NH_2, and *x* represents the number of such groups) film aerogel delivers a high mass specific capacitance of 560 F·g^{-1} and excellent cycling performance of 94.5% capacitance retention after 12,000 cycles in 0.5 M H_2SO_4. In addition, the flexible all-solid-state supercapacitor (ASC) composed of MXene film electrodes has excellent specific capacitance ~ 277 F·g^{-1} and high energy density ~ 52.8 Wh·kg^{-1} at 1600 W·kg^{-1}. Therefore, this work not only proposes a feasible synthetic method that can precisely regulate the pore structure and surface features of film aerogels, but also demonstrates the broad application prospects of aerogel materials in wearable power devices.

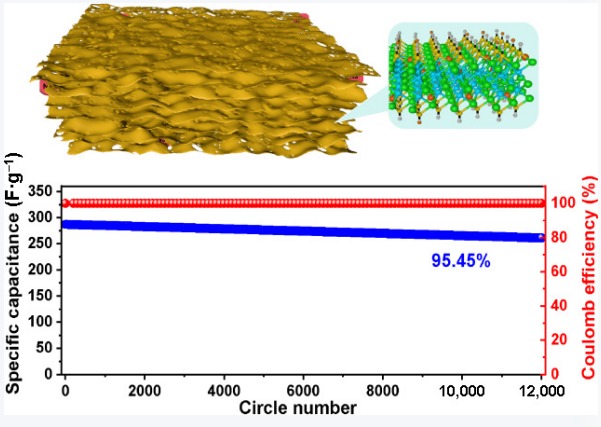

KEYWORDS: MXene, aerogel, intercalation, supercapacitors, capacitance

1 Instructions

Supercapacitors are well known as high performance energy storage devices due to their advantages of fast charging and discharging, long cycle life, high power density and environmental friendliness [1]. Currently, they have a wide range of applications in portable and wearable electronic devices, especially flexible supercapacitors, which have important applications in wearable electronics due to their high capacitance, long cycle life, low cost and flexibility [2, 3]. In general, electrode materials have a great influence on the electrochemical performance of capacitors and flexible energy storage devices [4–6]. Ideal flexible electrode materials should have high electrical conductivity, modulated pore size, interconnected pore structure and good mechanical flexibility [7]. Unfortunately, some inherent problems (e.g., poor long-term stability and inferior safety) have severely limited their industrial applications [8]. Therefore, developing advanced three-dimensional (3D) porous electrode materials with greatly improved cycling stability become a great challenging so far.

To the best of our knowledge, MXenes, as a class of popular two-dimensional (2D) materials, has received continuous attention due to good conductivity, high specific surface area and easy surface modification [7–12]. In which, the 2D layered structure of MXene provides ample interlayer space to accommodate a range of monovalent and multivalent cations. However, MXene nanosheets are susceptible to easy aggregation and self-stacking of nanolayers to form dense structures due to strong van der Waals interaction, leading to inefficient ion transport and deactivation of

Received: October 9, 2024; **Revised:** October 18, 2024
Accepted: October 22, 2024

✉Address correspondence to guoxh2009@nwu.edu.cn

electrochemically active sites within the MXene, which finally deacy its electrochemical performance [13–16]. Therefore, several strategies are needed to optimize the structure of MXene materials for efficient ion transport. Firstly, the MXene layer spacing was regulated by inserting Li^+, Na^+, and/or K^+ ions into the interlayers of MXene via using the mechanism of spontaneous electrostatic attraction between the MXene and cations. Wang et al. [17] reported that Li^+, Na^+ and K^+ into an Al^{3+} pre-intercalated MXene and the multi-ionic pre-intercalated MXene electrode had a capacitance of 250.80 mAh·g^{-1}, wherein, the pre-intercalation of Na^+ could keep the MXene in a more stable structure, which was favorable for enhancing the electrochemical cycling performance. Yuan et al. [18] found that enlarged the interlayer distance and shortened the diffusion path of sodium ions by constructing 3D folded MXene with pre-intercalation of Na^+, K^+ and Li^+ that can achieve a high reversible capacitance of 256 mAh·g^{-1} after 100 cycles and a long cycle stability of 6000 cycles. Ameer et al. [19] used X-ray absorption spectroscopy (XAS) to study the electronic structure of Li^+, Na^+, K^+ and Mg^{2+} intercalated MXenes and demonstrated that the cation insertion and the H_2SO_4 electrolyte environment affect the surface chemistry of $Ti_3C_2T_x$ (where T is –O, –OH, –F, and/or –NH_2, and x represents the number of such groups). In addition, study demonstrated that lower group concentrations lead to more Ti atoms participate in redox reactions, allowing MXene to exhibit excellent energy storage properties [20]. For example, Saha et al. [21] used an unconventional single-step atomic surface reduction (ASR) technique to achieve surface functionalization of MXene and the surface-modified MXene showed a significant improvement in both rate performance and cycling stability. However, there are fewer studies in the field of electrochemistry regarding amino modification [22] and thus the role of amino groups on the electrochemical properties of MXene has not been systematically investigated.

Aerogels are porous solid materials with high porosity, a layered 3D morphology and adjustable porosity [23]. Aerogels have the advantages of facilitating electrolyte penetration, shortening the ion diffusion distance and resisting the expansion and contraction stresses of electrodes in the field of energy storage [24]. The current synthetic method for aerogels makes it impossible to precisely control the porous structure and the template method inevitably produces structural defects when the template is removed, leading to poor structural integrity. In contrast, direct foaming of solids allows precise regulation of the pore structure without loss of mechanical properties by controlling the foaming time and temperature [25]. Therefore, converting MXene films into aerogels with porous network structures, which can retain their good mechanical properties and recoverable deformation characteristics and can be directly tested electrochemically without the addition of binder in supercapacitor. The mesopores and macropores generated by MXene film aerogels in interconnected layered skeletons can act as electrolyte buffer reservoirs to facilitate the shuttling of electrolyte and ion shuttling, allowing ions to pass through the channels with low resistance.

Based on the above consideration, we propose a solid-state foaming method to prepare a kind of novel amino-functionalized and Na^+ pre-intercalated $Ti_3C_2T_x$-MXene film aerogels. The obtained 3D $Ti_3C_2T_x$ MXene (denoted as Na-$Ti_3C_2T_x$) displays specific porosity, Na^+ pre-intercalation and surface amination modification features. Specially, the Na-$Ti_3C_2T_x$ film aerogels can deliver high specific capacitance of 560 F·g^{-1} in 0.5 M H_2SO_4, which is superior to most reported MXenes. In addition, the assembled flexible all-solid-state supercapacitor (ASC) has an excellent specific capacitance (128 F·g^{-1}) and a high energy density (52.8 Wh·kg^{-1} at 1600 W·kg^{-1}), demonstrating their promising application in wearable electronic fields.

2 Experimental methods

2.1 Preparation of few-layered $Ti_3C_2T_x$ MXene nanosheets

The preparation of Ti_3AlC_2 powder and $Ti_3C_2T_x$ MXene has been reported elsewhere [1]. Typically, 4 g of Ti_3AlC_2 powder was slowly added to the mixed LiF (1 g) and HCl (80 mL) solution, followed by sufficiently stirring at 60 °C for 48 h. Then, the precipitates were collected and washed with deionised water for several times until pH ~ 5, resulting in multilayered MXene nanosheets. Afterwards, the multilayered MXene nanosheets were added into 80 mL of dimethyl sulfoxide and ultrasonicated for 8 h, resulting in the final few-layered MXene nanosheets (13 mg·mL^{-1}).

2.2 Synthesis of Na^+ pre-intercalated $Ti_3C_2T_x$ film aerogel

Na^+ pre-intercalated $Ti_3C_2T_x$ MXene nanosheets (Na-Ti_3C_2) were prepared by electrostatic self-assembly method. Typically, 1 mL of NaCl (10 mmol·mL^{-1}) was added to 10 mL of few-layered MXene solution. After stirring for 4 h, the solution was centrifuged and washed several times with deionised water to obtain Na-Ti_3C_2. The collected Na-Ti_3C_2 was then pump-filtered into a membrane. Then it was heated in 50% N_2H_4 solution at 50 °C for 48 h. After cooling to room temperature, the 3D $Ti_3C_2T_x$ MXene aerogel film with Na^+ pre-intercalation was prepared by freeze-drying and then named as Na-$Ti_3C_2T_x$-50. For comparison, without adding NaCl in this step, the film aerogels were also prepared in the same way at 30, 50 and 70 °C and then named as $Ti_3C_2T_x$-30, $Ti_3C_2T_x$-50 and $Ti_3C_2T_x$-70, respectively. In addition, the few-layered Ti_3C_2 solution was taken directly and pump-filtered to form a film and then freeze-dried to obtain a Ti_3C_2 sample.

3 Results and discussion

Figure 1 depicts the synthesis of $Ti_3C_2T_x$ MXene film aerogels with Na^+ pre-intercalation and amino surface modification. First, selective etching of the Al layer from Ti_3AlC_2 can yield lamellar $Ti_3C_2T_x$ with surfaces terminated with –OH, –Cl and –F groups [26]. After that, NaCl was added to spontaneously insert Na^+ between the MXene layers to generate Na^+ pre-intercalated $Ti_3C_2T_x$ (Na-$Ti_3C_2T_x$). Then the Na-$Ti_3C_2T_x$ was subjected to foamed porosity and terminal group modification in N_2H_4 solution at 50 °C to obtain the Na-$Ti_3C_2T_x$ film aerogel. It was noted that, the foaming progress can be controlled by temperature and allowing fine tuning of the $Ti_3C_2T_x$ interlayer transport channel structure and interface.

Next, the crystal structures of Ti_3C_2, $Ti_3C_2T_x$-30, $Ti_3C_2T_x$-50, $Ti_3C_2T_x$-70 and Na-$Ti_3C_2T_x$-50 film aerogels were analyzed by X-ray diffraction (XRD) technique. The XRD patterns (Fig. 2(a)) show that the (002) peak of the Ti_3AlC_2 is shifted to a lower angle after etching and there are six major peaks (i.e., (002), (004), (006), (008), (0010) and (0012)) for MXene, which is consistent with previously reported result [26, 27]. Compared with direct freeze-dried Ti_3C_2 (1.35 nm), the layer spacing of the (002) plane of $Ti_3C_2T_x$-30, $Ti_3C_2T_x$-50, $Ti_3C_2T_x$-70 was slightly decreased after N_2H_4 foam reduction due to the change in the surface moiety of Ti_3C_2, which

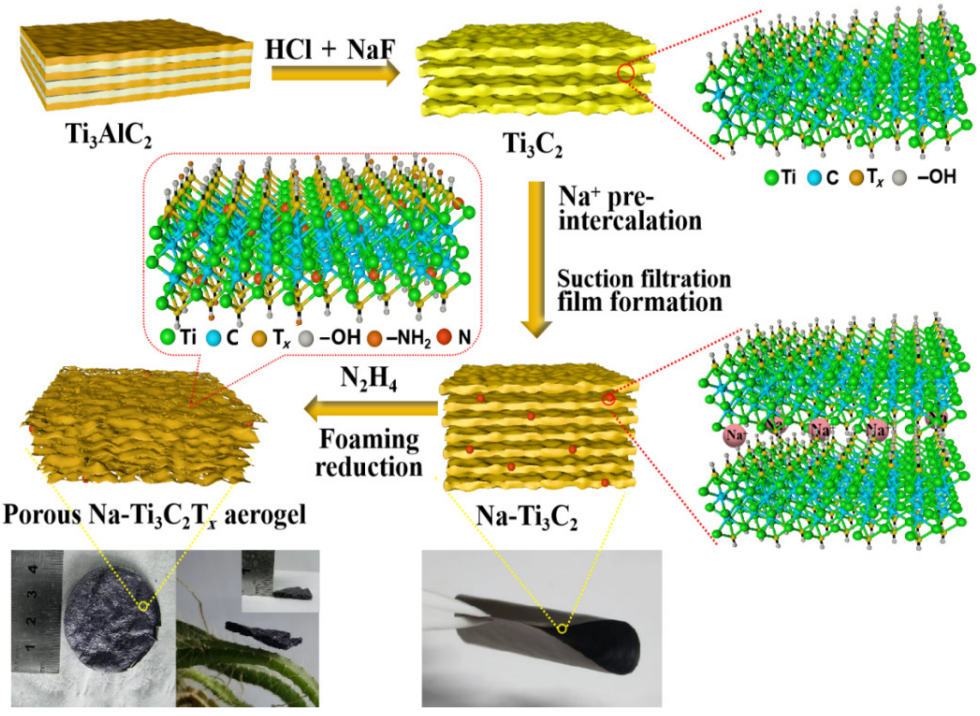

Figure 1 Schematic illustration of synthesis process and flexibility exhibition of Na-$Ti_3C_2T_x$-50 film aerogel.

result in the narrowing of the layer spacing. Na-$Ti_3C_2T_x$-50 has a layer spacing of 1.42 nm, which is much larger than that of Ti_3C_2 and $Ti_3C_2T_x$-50, suggesting the successful pre-intercalation of Na^+ into MXene framework.

In addition, the morphology and microstructure of $Ti_3C_2T_x$ film aerogels were investigated by scanning electron microscopy (SEM). The cross-sectional SEM images of pure Ti_3C_2 showed an irregularly lamellar structure (Fig. 2(b)). The cross-section of the MXene films after pore-forming through N_2H_4 at different temperatures showed 3D network-like structures with different thicknesses and the network structures of $Ti_3C_2T_x$-50 and Na-$Ti_3C_2T_x$-50 (thickness is about 400 μm) have a more ordered network structure (Figs. 2(c) and 2(d) and Figs. S1(a)–S1(d) in the Electronic Supplementary Material (ESM)), which is favorable for exposing more ion-accessible active sites. The surface SEM images of Ti_3C_2, $Ti_3C_2T_x$-30, $Ti_3C_2T_x$-50, $Ti_3C_2T_x$-70 and Na-$Ti_3C_2T_x$-50 film aerogels are shown in Figs. S2(a)–S2(e) in the ESM. After N_2H_4 reduction, small slices are appeared on MXenes. And the high-resolution transmission electron microscopy (HRTEM) images (Fig. 2(e)) of Na-$Ti_3C_2T_x$-50 show that the layer spacing is 1.4 nm and the lattice spacing is 0.23 nm, which is consistent with the XRD results. Energy dispersive spectroscopy (EDS) result further confirm that the uniform distribution of Na, N, F, Ti, C and O elements in Na-$Ti_3C_2T_x$-50 sample (Fig. 2(f)).

The isothermal N_2 adsorption/desorption testing were used to evaluate the specific surface area and pore size distribution of the erogel materials (Fig. 3). The specific surface areas of Ti_3C_2, $Ti_3C_2T_x$-50 and Na-$Ti_3C_2T_x$-50 were calculated to be 12.5, 30.6 and 45.2 $m^2 \cdot g^{-1}$ (Table S1 in the ESM), respectively, indicating that the foaming reduction of N_2H_4 and Na^+ pre-intercalation can effectively increase the specific surface area of the materials. The Ti_3C_2, $Ti_3C_2T_x$-50 and Na-$Ti_3C_2T_x$-50 exhibit typical type IV isotherms and significant H_2 hysteresis regions at medium and high pressures, suggesting the presence of abundant mesoporous structures (Fig. 3(a)) [5, 28, 29]. In addition, two steep peaks can be observed at both low and high relative pressures (P/P_0 < 0.02 and P/P_0 > 0.96), demonstrating the simultaneous presence of micro-and macropores [30, 31]. Figure 3(b) shows that compared to Ti_3C_2 (8.63 and 14.76 nm), $Ti_3C_2T_x$-50 and Na-$Ti_3C_2T_x$-50 have micropores with a size of 1.36 nm, mesopores with a size of 6.34 and 8.63 nm and macropore apertures with a size of 147.6 nm, suggesting that the foaming of N_2H_4 produces both micropores and mesopores and even macropore in Na-$Ti_3C_2T_x$. Furthermore, Na-$Ti_3C_2T_x$-50 has the highest micropore content (1.27%), indicating that Na^+ pre-intercalation contributes to the formation of micropores (Table S1 in the ESM). In addition, from Fig. S3 and Table S1 in the ESM, the pore size distributions of $Ti_3C_2T_x$-30 are 1.36, 7.4, 8.63 and 147.6 nm; the pore size distributions of $Ti_3C_2T_x$-50 are 1.36, 6.34, 8.63, 14.76 and 147.6 nm; and the pore size distributions of $Ti_3C_2T_x$-70 are 1.27, 8.63, 18.59 and 147.6 nm, respectively, suggesting that the mesoporous size can be controlled by controlling the reaction temperature.

Fourier transform infrared (FTIR) spectra further demonstrate the structure of the MXene films before and after N_2H_4 reduction (Fig. S4(a) in the ESM). The Ti_3C_2 and $Ti_3C_2T_x$-50 have two peaks at 1080 and 557 cm^{-1} , which are assigned to the surface groups of C–F and –OH, respectively [32–34]. The observed peaks at ~ 2820 cm^{-1} of Ti_3C_2 and $Ti_3C_2T_x$-50 are assigned to C–H asymmetric stretching mode [35]. The adsorption peak at ~ 1350 cm^{-1} is attributed to the bending of –OH groups [23] and the absorption peak at about 3200–3700 cm^{-1} are assigned to the tensile vibration of the hydroxyl group (–OH) [32, 36]. The absorption peak at 2904 cm^{-1} is derived from C–H stretching vibration [32]. The peak appearing at ~ 1400 cm^{-1} in the $Ti_3C_2T_x$-50 spectra correspond to C–N bending vibration [37].

Next, X-ray photoelectron spectroscopy (XPS) test was conducted to study the surface chemical properties of Ti_3C_2, $Ti_3C_2T_x$-50 and Na-$Ti_3C_2T_x$-50 aerogels, as shown in Fig. 4 and Figs. S4(b)–S4(f) in the ESM. The XPS full spectra of Ti_3C_2, $Ti_3C_2T_x$-50 and Na-$Ti_3C_2T_x$-50 film aerogels contain Ti 2p, C 1s, O 1s, F 1s

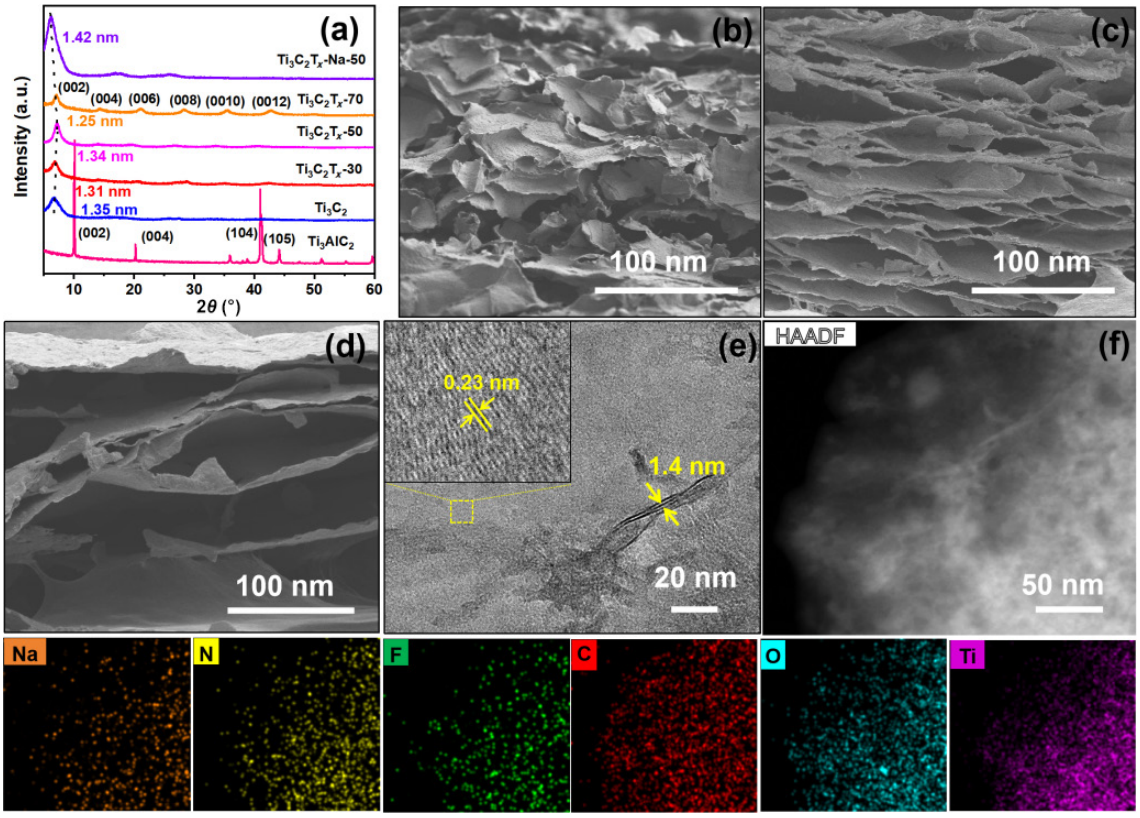

Figure 2 (a) XRD patterns of the pure foaming, $Ti_3C_2T_x$-30, $Ti_3C_2T_x$-50, $Ti_3C_2T_x$-70 and Na-$Ti_3C_2T_x$-50 film aerogels. (b) Cross-sectional SEM images of pure Ti_3C_2, (c) $Ti_3C_2T_x$-50 and (d) Na-$Ti_3C_2T_x$-50 film aerogels. (e) HRTEM images of Na-$Ti_3C_2T_x$-50, (f) TEM elemental mapping of Na-$Ti_3C_2T_x$-50 film aerogel.

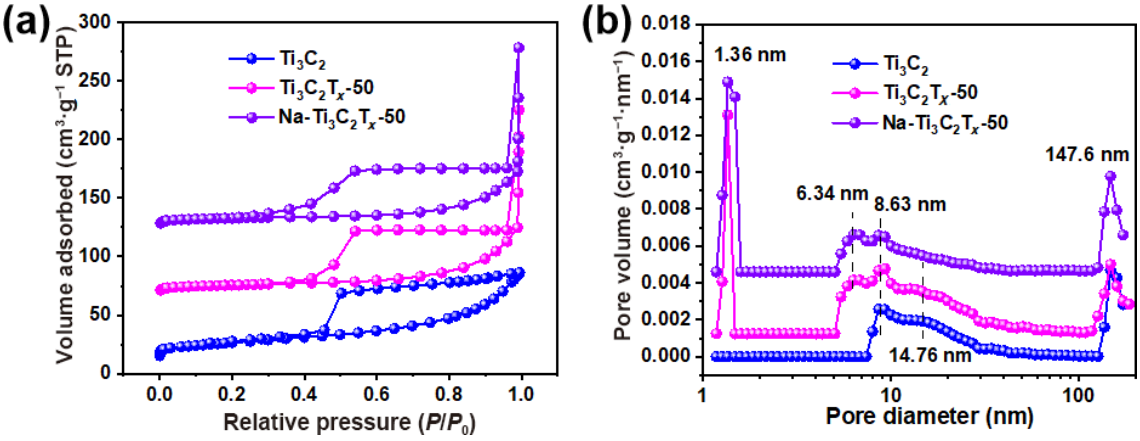

Figure 3 (a) Nitrogen adsorption–desorption isotherms and (b) pore size distributions of Ti_3C_2, $Ti_3C_2T_x$-50 and Na-$Ti_3C_2T_x$-50 film aerogels.

and Cl 2p peaks as shown in Figs. S4(b)–S4(f) in the ESM. $Ti_3C_2T_x$-50 and Na-$Ti_3C_2T_x$-50 film aerogels contain Ti 2p, C 1s, O 1s, F 1s and Cl 2p peaks as displayed in Fig. S4(b) in the ESM. Compared to Ti_3C_2, $Ti_3C_2T_x$-50 and Na-$Ti_3C_2T_x$-50 aerogels show the new peak N 1s at 400 eV [28], confirming that the successful doping of N atom in $Ti_3C_2T_x$. And the C–N and –NH_2 bonds in Fig. 4(a) and Fig. S4(c) in the ESM are coincide with the N 1s spectra in Fig. 4(b), demonstrating the successful N doping and partial –NH_2 function in $Ti_3C_2T_x$ [38]. As can be seen from Table S2 in the ESM, Figs. 4(c) and 4(d), and Figs. S4(c)–S4(f) in the ESM, compared with Ti_3C_2, the decrease in the percentage of C–Ti–F_x (from 33.60% to 27.20%) and C–Ti–$(OH)_x$ (from 50.90% to 38.30%) of $Ti_3C_2T_x$-50 decreased after N_2H_4 reduction is attributed to the additional formation of –NH_2 groups and substitution for some of end groups. Since the reduction of –F groups not only increase the crystal spacing, but also allow more Ti atom to form a stronger reoxidation reaction [39], which can help to improve the charge storage capacitance of MXene. The Na-$Ti_3C_2T_x$-50 aerogel showed Na KLL and Na 1s peaks at 500 and 1070 eV (Fig. S4(b) in the ESM and Fig. 4(e)) and the results confirmed that the Na atoms were successfully doped into $Ti_3C_2T_x$ [18, 40]. The deconvoluted Ti 2p spectra of Na-$Ti_3C_2T_x$-50 (Fig. 4(f)) were Ti-C $2p_{3/2}$, Ti^{2+}/Ti^{3+} $2p_{3/2}$, Ti–O $2p_{3/2}$, Ti–C $2p_{3/2}$, Ti^{2+}/Ti^{3+} $2p_{3/2}$ and Ti–O $2p_{3/2}$, which were located at 455.58, 456.27, 457.47, 459.59, 462.01 and 464.32 eV. The Ti 2p spectra of Ti_3C_2, $Ti_3C_2T_x$-50 (Fig. S4(d) in the ESM) and Na-$Ti_3C_2T_x$-50 are in agreement with previous reports [11, 16]. Compared to Ti_3C_2, the Ti $2p_{3/2}$ and Ti $2p_{1/2}$ peaks of $Ti_3C_2T_x$-50 and Na-$Ti_3C_2T_x$-50 are shifted towards lower binding energy, which

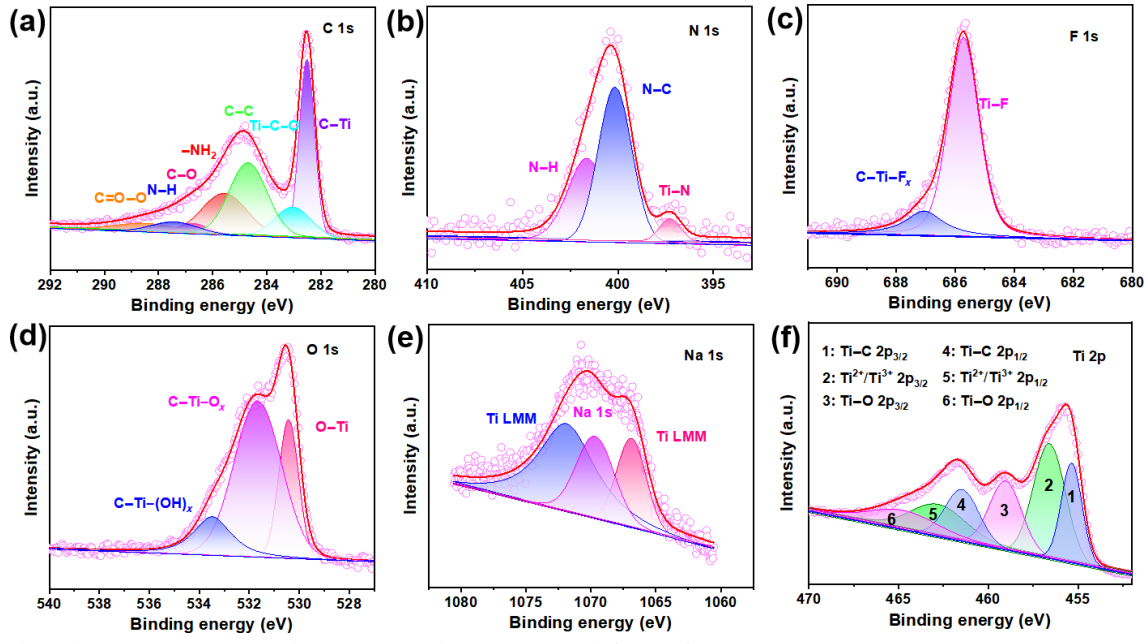

Figure 4 High-resolution XPS spectra (a) C 1s, (b) N 1s, (C) F 1s, (d) O 1s, (e) Na 1s and (f) Ti 2p of Na-$Ti_3C_2T_x$-50.

is due to the $-NH_2$ functionalism and the pre-intercalation of Na^+ [17, 27]. Notably, the C–Ti–$(OH)_x$ peaks of $Ti_3C_2T_x$-50 were shifted towards lower binding energy compared to Ti_3C_2 due to the greater electronegativity of $-NH_2$ that result in the transfer of more electrons from Ti to N (Fig. S4(f) in the ESM). In particular, due to the strong electrostatic interactions between Na^+ and the negatively charged groups of the adjacent MXene sheets, the binding energy of Na-$Ti_3C_2T_x$-50 is positively shifted and ionic bonds are formed between the layers of MXene sheets (Fig. 4(d)), leading to a redistribution of electrons [4].

The electrochemical performance of Ti_3C_2, $Ti_3C_2T_x$-30, $Ti_3C_2T_x$-50 $Ti_3C_2T_x$-70 and Na-$Ti_3C_2T_x$-50 samples was carried out via using a three-electrode system in 0.5 M H_2SO_4 electrolyte. The cyclic voltammetry (CV) curves of all samples within a potential window of −0.5 to 0.1 V (vs. Ag/AgCl) at a scan rate of 10 mV·s^{-1} are shown in Fig. 5(a) and redox peaks can be clearly seen at −0.15/−0.4 V. Typical CV and galvanostatic charge–discharge (GCD) curves of Na-$Ti_3C_2T_x$-50 at different scan rates and different current densities are shown in Figs. 5(b) and 5(c). In addition, the CV and GCD curves of Ti_3C_2, $Ti_3C_2T_x$-30, $Ti_3C_2T_x$-50 and $Ti_3C_2T_x$-70 are presented in Figs. S5(a)–S5(h) in the ESM. Obviously, the CV curves of all the samples show similar irregular rectangles and obvious redox peak at 10–40 mV·s^{-1}, indicating that the charge storage at low sweeping speeds mainly comes from the pseudocapacitive effect [9, 41, 42]. In addition, the GCD curves of all the samples are almost curved triangles instead of flat straight lines, indicating the pseudocapacitive property. In the H_2SO_4 electrolyte, the redox peaks of MXene are mainly originated from the bonding/decoupling of hydrated hydrogen ions with terminal oxygen-containing groups in the electrode, which further changed the valence state of elemental Ti. The details are described as follows

$$Ti_3C_2O_x(OH)_yF_z + \delta e^- + \delta H^+ \rightarrow Ti_3C_2O_{x-\delta}(OH)_{y+\delta} + F_z \quad (1)$$

$$Ti_3C_{2-x}N_x + \delta e^- + \delta H^+ \rightarrow Ti_3C_{2-x}N_xH_\delta \quad (2)$$

$$Ti_3C_{2-x}(NH_2)_x + \delta e^- + \delta H^+ \rightarrow Ti_3C_{2-x}O_{x-\delta}(NH_2)_xH_\delta \quad (3)$$

In addition, the integral area of CV curves and the discharge time of the GCD curves obey the following order: Ti_3C_2 < $Ti_3C_2T_x$-50 < Na-$Ti_3C_2T_x$-50, indicate that N doping, $-NH_2$ functionalization and Na^+ pre-intercalation are effective in improving the specific capacitance of MXene. The GCD curves of Na-$Ti_3C_2T_x$-50 at various densities of 1–20 A·g^{-1} is shown in Fig. 5(c). The curves exhibit a curved triangle, which is consistent with the description of the above CV curves, in addition to the high symmetry of the curve indicate good electrochemical reversibility. The GCD curves obtained the specific capacitance by weight of all the materials at different current densities are shown in Fig. 5(d). The Na-$Ti_3C_2T_x$-50 film aerogel electrode material has the highest specific capacitance of 560 F·g^{-1} at 1 A·g^{-1}, while Ti_3C_2, $Ti_3C_2T_x$-30, $Ti_3C_2T_x$-50 and $Ti_3C_2T_x$-70 have 258, 312, 363 and 417 F·g^{-1}, respectively. Interestingly, the obtained area specific capacitance of all samples as shown in Fig. S5(i) in the ESM follows the same trend with the weight specific capacitance. The high specific capacitance of the Na-$Ti_3C_2T_x$-50 film aerogel suggests that the specific capacitance of the MXene material can be further improved by the synergistic effect of heteroatom doping, functional group modification and the construction of a new 3D porous network structure. Moreover, the obtained Na-$Ti_3C_2T_x$-50 film aerogel is superior to other MXene-based materials reported in the literature as supercapacitor electrode materials (Table S3 in the ESM). The Na-$Ti_3C_2T_x$-50 film aerogel was evaluated by repeating the GCD test at 10 A·g^{-1}. The results showed that the specific capacitance only decreased to 95.45% after 12,000 cycles (Fig. 5(e)), indicating robust cycling stability. The SEM images after cycling are shown in Fig. S7 in the ESM and the cycled Na-$Ti_3C_2T_x$-50 electrode retained a good lamellar structure without obvious collapse and some by-products were generated on the surface. Figure S8 in the ESM compares the XRD patterns of Na-$Ti_3C_2T_x$-50 before and after cycling. The diffraction peak of Ti_3C_2 did not disappear after cycling, but the diffraction peak of Na_2TiO_3 appeared. This is owing to the unavoidable oxidation reaction of Ti_3C_2 in the air environment at long time cycling test, meanwhile the oxidized TiO_2 combines with

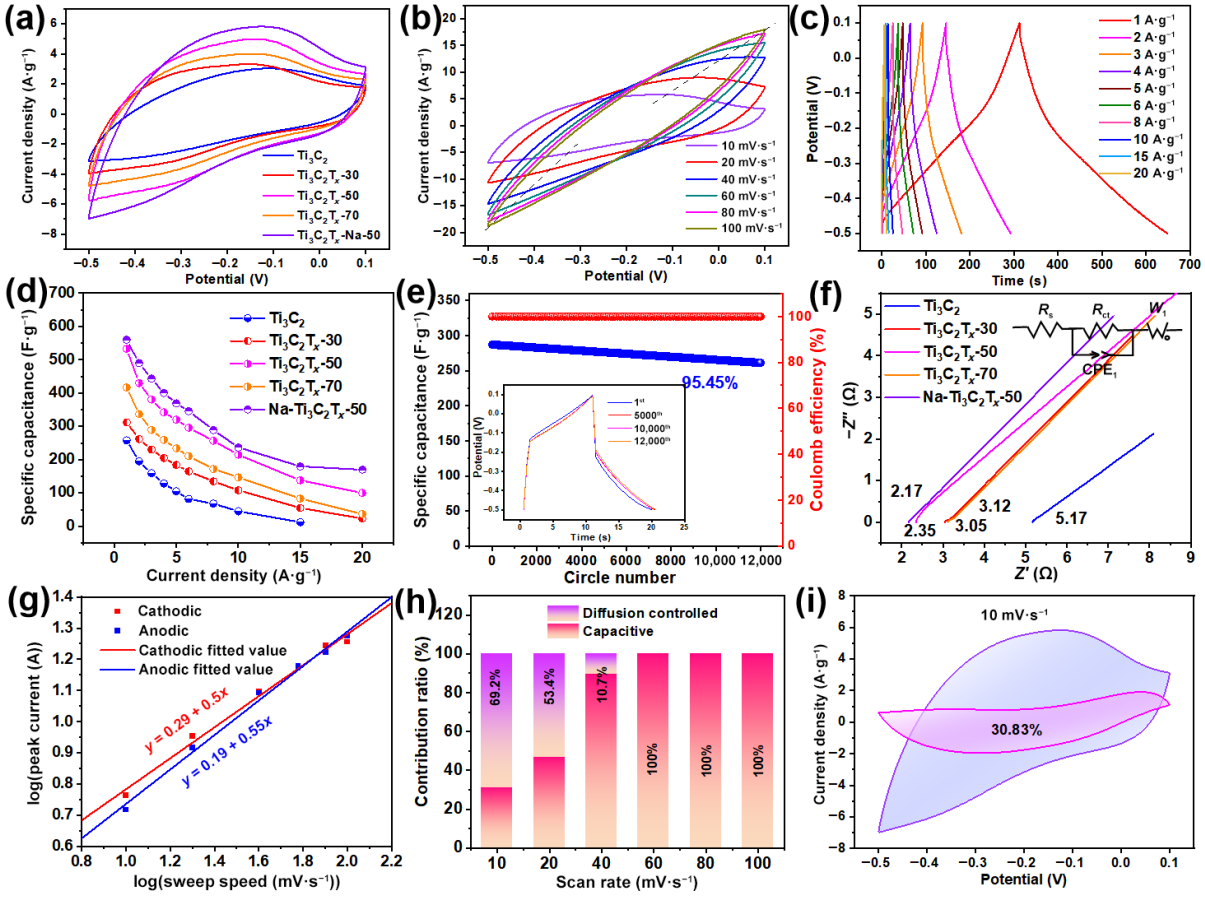

Figure 5 Electrochemical performance of all samples in 0.5 M H_2SO_4 electrolyte. (a) Comparison of CV curves of all samples at 10 mV·s^{-1}. (b) CV and (c) GCD curves of Na-$Ti_3C_2T_x$-50. (d) Plots of gravimetric capacitance versus current density for samples, (e) cycling stability and coulombic efficiency of Na-$Ti_3C_2T_x$-50 measured at 10 A·g^{-1} after 12,000 cycles (the inset showing the charge–discharge curves before and after 12,000 cycles). (f) Nyquist impedance plots of all samples. (g) The *b*-value of samples and (h) contribution of diffusion and capacitance processes to the total capacitance of Na-$Ti_3C_2T_x$-50 at different scanning speeds. (i) The surface capacitive contributions illustrated in CV curves of Na-$Ti_3C_2T_x$-50 at 10 mV·s^{-1}.

Na^+. In addition, the peaks of the samples after cycling are slightly shifted to a large angle, which may be due to a slight decrease in the layer spacing as a result of the generation of by-products during the cycling process.

In order to investigate the charge transport kinetics of Na-$Ti_3C_2T_x$-50, we performed electrochemical impedance spectroscopy (EIS) tests. The Nyquist plot fitted by the equivalent circuit model (consisting of an internal resistance R_s, a constant phase element CPE_1 (CPE: constant phase element), a charge transfer resistance R_{ct} and a Warberg impedance W_1) is shown in Fig. 5(f). In the high frequency region, the real axis intercept of the Nyquist plot is used to determine R_s. The value of R_s is related to the sum of the electrode/electrolyte interface resistance and the electrode material resistance. The R_s of Ti_3C_2, $Ti_3C_2T_x$-50 and Na-$Ti_3C_2T_x$-50 were measured to be 5.17, 2.35 and 2.17 Ω, respectively, suggesting that the $-NH_2$ and Na^+ pre-intercalation layers altered the electronic structure of the materials and improved their electrical conductivity. The Ti_3C_2, $Ti_3C_2T_x$-50 and Na-$Ti_3C_2T_x$-50 (0.01, 0.03 and 0.05 Ω) have lower R_{ct} values due to the 3D porous structure and the direct use of the film aerogel as an electrode that improve the contact between the electrode and electrolyte. In addition, the samples of $Ti_3C_2T_x$-50 and Na-$Ti_3C_2T_x$-50 have higher slopes in the low frequency region compared to Ti_3C_2, suggesting that the 3D network structure render them superior charge transfer properties and lower diffusion resistance.

To further investigate the charge storage and ion transport mechanism of the material, the effects of the diffusion-controlled and capacitive contributions on the total charge storage were further analyzed. $i = av^b$, where i is the peak current, v is the scan rate, a is a variable parameter and b values of 1 and 0.5 represent the capacitive surface-controlled process and the diffusion-controlled Faraday redox process, respectively [43]. Figure 5(g) and Figs. S6(a), S6(c), S6(e) and S6(g) in the ESM show plots of log$i$ versus log$v$ from 10 to 100 mV·s^{-1}. The results show that the b values of Ti_3C_2, $Ti_3C_2T_x$-30, $Ti_3C_2T_x$-50, $Ti_3C_2T_x$-70 and Na-$Ti_3C_2T_x$-50 samples are 0.49/0.57, 0.57/0.63, 0.43/0.51, 0.60/0.61 and 0.5/0.55, respectively. The b values are all close to 0.5, suggesting that diffusion controlled processes dominate their total capacitance. Where, v is the specific scanning rate and $i(V)$ is the current at a fixed potential. The k_1v and $k_2v^{1/2}$ represent the capacitance-controlled and diffusion-controlled currents, respectively. Therefore, Fig. 5(h) and Figs. S6(b), S6(d), S6(f) and S6(h) in the ESM demonstrate the specific contributions of the capacitance-controlled and diffusion-controlled currents calculated by k_1v and $k_2v^{1/2}$ at different scanning rates. The capacitance-controlled and diffusion-controlled capacitance contributions of the Ti_3C_2, $Ti_3C_2T_x$-30, $Ti_3C_2T_x$-50, $Ti_3C_2T_x$-70 and Na-$Ti_3C_2T_x$-50 thin-film aerogels at 10 mV·s^{-1} display diffusion-controlled capacitance contributions of 71.4%, 79.9%, 61.2%, 77% and 69.2% (Fig. 5(i)), respectively. In addition, the diffusion control capacitance contribution increases as

the current density decreases, mainly because the electrolyte ions can fully bind to the active sites during the diffusion process, thus effectively increase the diffusion capacitance. Based on the above experimental results, we speculated the reasons for the enhanced electrochemical performance of Na-$Ti_3C_2T_x$-50. According to the literature, the protonation process of oxygen-containing functional groups occurs under acidic conditions, which facilitates the electrochemical reaction [4, 20, 26]. Herein, N_2H_4 reduction leads to N-doping and amino group substitution of some oxygen-containing functional groups, which can provide more electrochemical reactive sites and favor pseudocapacitive reactions during electrochemical processes. Adjacent MXene nanosheets disrupt the interlayer Coulomb force through Na^+, increasing the interlayer spacing and forming a 3D structure with more active sites, which increase electrolyte accessibility and optimze the electronic structure and improve the electron transfer efficiency. As a result, the specific capacitance of MXene supercapacitors is significantly improved.

To verify the the practical application feasibility of MXene film aerogels in the field of energy storage, we prepared flexible asymmetric solid-state supercapacitors by employing H_2SO_4/poly(acrylic acid) (PAA) gel as the gel electrolyte and Ti_3C_2, $Ti_3C_2T_x$-50 and Na-$Ti_3C_2T_x$-50 aerogels and acetylene black (AC) as the electrodes, respectively. The CV curves were tested in different potential windows of 0–1.4, 0–1.6 and 0–1.8 V with a sweep rate of 100 mV·s^{-1}. As shown in Fig. 6(a), the devices exhibited a similar rectangular shape at the optimal voltage window of 0–1.6 V. In addition, the CV curves exhibited an approximately rectangular shape as the sweep rate increased (Fig. 6(b)). The performance of the device was then tested at different current densities (Fig. 6(c)) and the GCD curves were quasi-triangular, indicating the insertion pseudo-capacitive behaviour of the device. The specific capacitance of all samples are shown in Fig. 6(d) and the weight specific capacitance of the devices were 277 and 37 F·g^{-1} at current densities of 1 and 6 A·g^{-1}, respectively. Figure 6(e) and Fig. S9 in the ESM show the Ragone diagram of the flexible ASCs. According to the calculation, our flexible ASCs Na-$Ti_3C_2T_x$-50//AC exhibits an excellent mass energy density of 52.8 Wh·kg^{-1} at a power density of 1600 W·kg^{-1} and volumetric energy density of 37.76 Wh·L^{-1} at 1142.3 W·L^{-1}, which are obviously higher than that of the currently reported MXene-based asymmetric supercapacitors, such as MXene/NiCo-layered double hydroxides (LDHs) [42] (14.2 Wh·kg^{-1} at 3007.1 W·kg^{-1}), 3D $Ti_3C_2T_x$ MXene film [44] (9.55 Wh·kg^{-1} at 603.16 W·kg^{-1}), Ti_2CT_x@polyaniline [6] (42.3 Wh·kg^{-1} at 950 W·kg^{-1}), S, N-reduced graphene oxide (rGO)@MXene [45] (24.2 Wh·kg^{-1} at 1400.6 W·kg^{-1}). A total of 10,000 consecutive charge/discharge cycles were performed at 6 A·g^{-1} (Fig. 6(f)) to evaluate the long cycling stability of the Na-$Ti_3C_2T_x$-50//AC device. Specially, the capacitance retention of 61.1% can be obtained after 10,000 cycles, the Na-$Ti_3C_2T_x$-50//AC device demonstrates good cycling stability. To further verify the practical application feasibility of the Na-$Ti_3C_2T_x$-50//AC device, we connect two devices in parallel and series to extend the operating voltage window and capacitance. As shown in Fig. 6(g), when two devices are connected in series, the voltage window is extended to 2.4 V and then the parallel connection can double the capacitance.

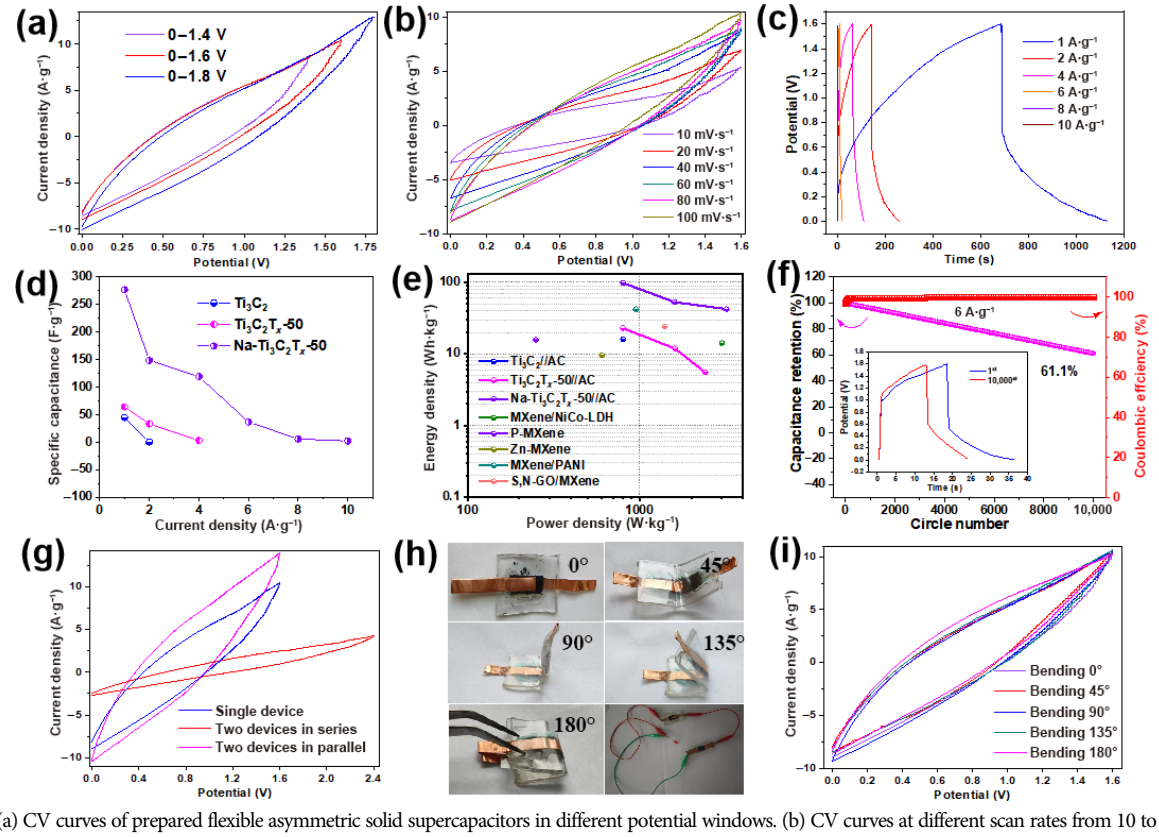

Figure 6 (a) CV curves of prepared flexible asymmetric solid supercapacitors in different potential windows. (b) CV curves at different scan rates from 10 to 100 mV·s^{-1}. (c) GCD curves obtained at current density from 0.5 to 5 A·g^{-1}. (d) Mass capacitances of devices. (e) Ragone plots of Ti_3C_2//AC, $Ti_3C_2T_x$-50//AC and Na-$Ti_3C_2T_x$-50//AC flexible ASCs. (f) Capacitance retention of Na-$Ti_3C_2T_x$-50//AC devices after 10,000 cycles (the inset showing the charge–discharge curves before and after 10,000 cycles). (g) CV curves of the two Na-$Ti_3C_2T_x$-50//AC devices in series and parallel. (h) Optical photos of devices at different angles and demonstration of LED using our Na-$Ti_3C_2T_x$-50-based supercapacitor. (i) CV curves of devices at different angles.

Importantly, our MXene-based device can light up a red light-emitting diode (LED), as shown in Fig. 6(h). In addition, flexibility is an important aspect for flexible ASCs. Figure 6(i) shows the CV curves at different bending angles at a scan rate of 100 mV·s^{-1}. The CV curves at 0°, 45° , 90°, 135° and even 180° bending are well overlapped. This demonstrates the potential advantages of its excellent mechanical and capacitance and stability in flexible electronic devices.

4 Conclusions

In summary, a novel kind of amino-functionalized and Na^+ pre-intercalated MXene film aerogels has been synthesized by solid foaming method. The synergistic effect of Na^+ pre-intercalation and $-NH_2$ functional group can significantly increase the interlayer spacing and change the electronic structure of MXene, thereby improving its electrochemical performance in H_2SO_4 electrolyte. Specially, the MXene-based 3D network structure can expose a large amount of active sites and accelerate electron transport that can greatly enhance its storage energy capability. And hence, the Na-$Ti_3C_2T_x$-50 film aerogel can achieve a high mass specific capacitance of 560 F·g^{-1} and an ultra-high cycle performance (94.5%) after 12,000 cycles in 0.5 M H_2SO_4. In addition, the flexible solid-state supercapacitor composed of MXene film electrode has excellent specific capacitance (128 F·g^{-1}) and high energy density ~ 52.8 Wh·kg^{-1} at 1600 W·kg^{-1}. These interesting findings would provide feasible strategy and/or solutions for the development of advanced MXene aerogel-based electrode materials in future storage energy-related applications.

Electronic Supplementary Material: Supplementary material (electrochemical measurements, SEM, Brunauer–Emmett–Teller (BET), FTIR, XPS and electrochemical information of film aerogels; Figs. S1–S9 and Tables S1–S3) is available in the online version of this article at https://doi.org/10.26599/NR.2025.94907092.

Data availability

All data needed to support the conclusions in the paper are presented in the manuscript and the Electronic Supplementary Material. Additional data related to this paper may be requested from the corresponding author upon request.

Acknowledgements

This work was supported by the Key projects of intergovernmental international cooperation in key R & D programs of the Ministry of science and technology of China (No. 2021YFE0115800), the National Science Funding Committee of China (No. U20A20250), the programs of the science and technology of Yulin City (No. CXY-2023-ZX04) and the funding support from Shccig-Qinling Program.

Declaration of competing interest

The authors declare no competing financial interest.

Author contribution statement

X. H. J. performed the experimental characterization and paper writing. D. J. M., L. R. F., and D. W. were involved in part data analysis. B. L. S. and X. H. G. supervised, guided and reviewed the work. All authors contributed to the general discussion.

Use of AI statement

None.

References

[1] Xu, W. T.; Xu, Z.; Liang, Y. X.; Liu, L. M.; Weng, W. Enhanced tensile and electrochemical performance of MXene/CNT hierarchical film. *Nanotechnology* **2021**, *32*, 355706.

[2] Li, H. Z.; Du, T. Y.; Wang, Q.; Guo, J. Y.; Zhang, S. Y.; Lu, Y. A new synthesis of O/N-doped porous carbon material for supercapacitors. *J. Energy Storage* **2023**, *66*, 107397.

[3] Zhang, Y. H.; Shang, Z.; Shen, M. X.; Chowdhury, S. P.; Ignaszak, A.; Sun, S. H.; Ni, Y. H. Cellulose nanofibers/reduced graphene oxide/polypyrrole aerogel electrodes for high-capacitance flexible all-solid-state supercapacitors. *ACS Sustain. Chem. Eng.* **2019**, *7*, 11175–11185.

[4] Zhou, L.; Zhang, J.; Wu, Y. Q.; Wang, W. X.; Ming, H.; Sun, Q. J.; Wang, L. M.; Ming, J.; Alshareef, H. N. Understanding ostwald ripening and surface charging effects in solvothermally-prepared metal oxide-carbon anodes for high performance rechargeable batteries. *Adv. Energy Mater.* **2019**, *9*, 1902194.

[5] Li, Q.; Cao, Z.; Cheng, H. R.; Zhang, J. L.; Ma, Z.; Wahyudi, W.; Cavallo, L.; Sun, Q. J.; Ming, J. Electrolyte boosting microdumbbell-structured alloy/metal oxide anode for fast-charging sodium-ion batteries. *ACS Materials Lett.* **2022**, *4*, 2469–2479.

[6] Fu, J. J.; Yun, J.; Wu, S. X.; Li, L.; Yu, L. T.; Kim, K. H. Architecturally robust graphene-encapsulated MXene Ti_2CT_X@polyaniline composite for high-performance pouch-type asymmetric supercapacitor. *ACS Appl. Mater. Interfaces* **2018**, *10*, 34212–34221.

[7] Xiao, Z. M.; Sun, K. S.; Zheng, Y.; Pang, J. X.; Gu, T. T.; Kong, W. W.; Chen, L. Implementation of high-capacity 3D $Ti_3C_2T_X$ MXene supercapacitors with terminal group modification. *ACS Appl. Mater. Interfaces* **2023**, *15*, 51151–51159.

[8] Yang, C. H.; Tang, Y.; Tian, Y. P.; Luo, Y. Y.; Faraz Ud Din, M.; Yin, X. T.; Que, W. X. Flexible nitrogen-doped 2D titanium carbides (MXene) films constructed by an *ex situ* solvothermal method with extraordinary volumetric capacitance. *Adv. Energy Mater.* **2018**, *8*, 1802087.

[9] Dall'Agnese, Y.; Lukatskaya, M. R.; Cook, K. M.; Taberna, P. L.; Gogotsi, Y.; Simon, P. High capacitance of surface-modified 2D titanium carbide in acidic electrolyte. *Electrochem. Commun.* **2014**, *48*, 118–122.

[10] Liang, K.; Matsumoto, R. A.; Zhao, W.; Osti, N. C.; Popov, I.; Thapaliya, B. P.; Fleischmann, S.; Misra, S.; Prenger, K.; Tyagi, M. et al. Engineering the interlayer spacing by pre-intercalation for high performance supercapacitor MXene electrodes in room temperature ionic liquid. *Adv. Funct. Mater.* **2021**, *31*, 2104007.

[11] Ren, S.; Xu, J. L.; Cheng, L.; Gao, X.; Wang, S. D. Amine-assisted delaminated 2D $Ti_3C_2T_X$ MXenes for high specific capacitance in neutral aqueous electrolytes. *ACS Appl. Mater. Interfaces* **2021**, *13*, 35878–35888.

[12] Cai, C. Y.; Wei, Z. C.; Deng, L. X.; Fu, Y. Temperature-invariant superelastic multifunctional MXene aerogels for high-performance photoresponsive supercapacitors and wearable strain sensors. *ACS Appl. Mater. Interfaces* **2021**, *13*, 54170–54184.

[13] Li, J.; Yuan, X. T.; Lin, C.; Yang, Y. Q.; Xu, L.; Du, X.; Xie, J. L.; Lin, J. H.; Sun, J. L. Achieving high pseudocapacitance of 2D titanium carbide (MXene) by cation intercalation and surface modification. *Adv. Energy Mater.* **2017**, *7*, 1602725.

[14] Hu, M. M.; Zhang, H.; Hu, T.; Fan, B. B.; Wang, X. H.; Li, Z. J. Emerging 2D MXenes for supercapacitors: Status, challenges and prospects. *Chem. Soc. Rev.* **2020**, *49*, 6666–6693.

[15] Xu, J. S.; You, J. H.; Wang, L.; Wang, Z. Y.; Zhang, H. Z. MXenes serving aqueous supercapacitors: Preparation, energy storage mechanism and electrochemical performance enhancement. *Sustain. Mater. Technol.* **2022**, *33*, e00490.
[16] Li, K. L.; Zhang, P.; Soomro, R. A.; Xu, B. Alkali-induced porous MXene/carbon nanotube-based film electrodes for supercapacitors. *ACS Appl. Nano Mater.* **2022**, *5*, 4180–4186.
[17] Wang, Y.; Li, J. M.; Han, W. J.; Zhao, C. M.; Xu, S. C.; Wang, D.; Yu, Z. L.; Lu, M.; Li, H. B.; Zhang, M. Z. Multi-ion competition mechanism within MXene interlayer and Li ion intercalated electrode function. *Appl. Surf. Sci.* **2023**, *623*, 157043.
[18] Yuan, Z. X.; Ju, S. L.; Li, W. Q.; Guo, H. N.; Chen, K.; Yue, M. Y.; Yu, X. B.; Wang, Y. J. Alkali ions pre-intercalated 3D crinkled $Ti_3C_2T_x$ MXene architectures for advanced sodium storage. *Chem. Eng. J.* **2022**, *450*, 138453.
[19] Al-Temimy, A.; Prenger, K.; Golnak, R.; Lounasvuori, M.; Naguib, M.; Petit, T. Impact of cation intercalation on the electronic structure of $Ti_3C_2T_x$ MXenes in sulfuric acid. *ACS Appl. Mater. Interfaces* **2020**, *12*, 15087–15094.
[20] Liu, L. Y.; Raymundo-Piñero, E.; Sunny, S.; Taberna, P. L.; Simon, P. Role of surface terminations for charge storage of $Ti_3C_2T_x$ MXene electrodes in aqueous acidic electrolyte. *Angew. Chem., Int. Ed.* **2024**, *63*, e202319238.
[21] Saha, A.; Shpigel, N.; Rosy; Leifer, N.; Taragin, S.; Sharabani, T.; Aviv, H.; Perelshtein, I.; Nessim, G. D.; Noked, M. et al. Enhancing the energy storage capabilities of $Ti_3C_2T_x$ MXene electrodes by atomic surface reduction. *Adv. Funct. Mater.* **2021**, *31*, 2106294.
[22] Moatasim, M.; Wang, Z. X.; Xie, Y. T.; Huang, H. C.; Chen, N. J.; Wang, Y. C.; Zhao, H. B.; Zhang, H. T.; Yang, W. Q. Solving gravimetric-volumetric capacitive paradox of 2D materials through dual-functional chemical bonding-induced self-constructing graphene-MXene monoliths. *ACS Appl. Mater. Interfaces* **2021**, *13*, 6339–6348.
[23] Lu, Z. Q.; Jia, F. F.; Zhuo, L. H.; Ning, D. D.; Gao, K.; Xie, F. Micro-porous MXene/aramid nanofibers hybrid aerogel with reversible compression and efficient EMI shielding performance. *Compos. B: Eng.* **2021**, *217*, 108853.
[24] Huang, X. W.; Huang, J. H.; Yang, D.; Wu, P. Y. A multi-scale structural engineering strategy for high-performance MXene hydrogel supercapacitor electrode. *Adv. Sci.* **2021**, *8*, 2101664.
[25] Pang, K.; Song, X.; Xu, Z.; Liu, X. T.; Liu, Y. J.; Zhong, L.; Peng, Y. X.; Wang, J. X.; Zhou, J. Z.; Meng, F. X. et al. Hydroplastic foaming of graphene aerogels and artificially intelligent tactile sensors. *Sci. Adv.* **2020**, *6*, eabd4045.
[26] Shao, H.; Xu, K.; Wu, Y. C.; Iadecola, A.; Liu, L. Y.; Ma, H. Y.; Qu, L. T.; Raymundo-Piñero, E.; Zhu, J. X.; Lin, Z. E. et al. Unraveling the charge storage mechanism of $Ti_3C_2T_x$ MXene electrode in acidic electrolyte. *ACS Energy Lett.* **2020**, *5*, 2873–2880.
[27] Li, L.; Zhang, M. Y.; Zhang, X. T.; Zhang, Z. G. New Ti_3C_2 aerogel as promising negative electrode materials for asymmetric supercapacitors. *J. Power Sources* **2017**, *364*, 234–241.
[28] Hu, B.; Shang, X. H.; Nie, P. F.; Zhang, B. S.; Xu, K. B.; Yang, J. M.; Qiu, J. S.; Liu, J. Y. Facile fabrication of a highly porous N-doped nanotubular carbon aerogel by an *in situ* template-growth method for high-performance supercapacitors. *ACS Appl. Energy Mater.* **2021**, *4*, 6991–7001.
[29] Wang, P. X.; Zhang, Y.; Yin, Y. Y.; Fan, L. S.; Zhang, N. Q.; Sun, K. N. *In situ* synthesis of $CuCo_2S_4$@N/S-doped graphene composites with pseudocapacitive properties for high-performance lithium-ion batteries. *ACS Appl. Mater. Interfaces* **2018**, *10*, 11708–11714.
[30] Xie, L. J.; Su, F. Y.; Xie, L. F.; Li, X. M.; Liu, Z.; Kong, Q. Q.; Guo, X. H.; Zhang, Y. Y.; Wan, L.; Li, K. X. et al. Self-assembled 3D graphene-based aerogel with Co_3O_4 nanoparticles as high-performance asymmetric supercapacitor electrode. *ChemSusChem* **2015**, *8*, 2917–2926.
[31] Zhao, Q.; Zhu, Q. Z.; Miao, J. W.; Zhang, P.; Wan, P. B.; He, L. Z.; Xu, B. Flexible 3D porous MXene foam for high-performance lithium-ion batteries. *Small* **2019**, *15*, 1904293.
[32] Xin, W.; Ma, M. G.; Chen, F. Silicone-coated MXene/cellulose nanofiber aerogel films with photothermal and joule heating performances for electromagnetic interference shielding. *ACS Appl. Nano Mater.* **2021**, *4*, 7234–7243.
[33] Cai, G. N.; Yu, Z. Z.; Tong, P.; Tang, D. P. Ti_3C_2 MXene quantum dot-encapsulated liposomes for photothermal immunoassays using a portable near-infrared imaging camera on a smartphone. *Nanoscale* **2019**, *11*, 15659–15667.
[34] Ai, F. R.; Fu, C. J.; Cheng, G. J.; Zhang, H. H.; Feng, Y. C.; Yan, X. L.; Zheng, X. J. Amino-functionalized Ti_3C_2 MXene quantum dots as photoluminescent sensors for diagnosing histidine in human serum. *ACS Appl. Nano Mater.* **2021**, *4*, 8192–8199.
[35] Meng, X. Y.; Sun, Y. F.; Yu, M. Z.; Wang, Z. Y.; Qiu, J. S. Hydrogen-bonding crosslinking MXene to highly robust and ultralight aerogels for strengthening lithium metal anode. *Small Sci.* **2021**, *1*, 2100021.
[36] Li, N.; Wei, X. Y.; Mei, Z.; Xiong, X. L.; Chen, S. M.; Ye, M.; Ding, S. G. Synthesis and characterization of a novel polyamidoamine-cyclodextrin crosslinked copolymer. *Carbohydr. Res.* **2011**, *346*, 1721–1727.
[37] Zhou, L.; Wu, F. M.; Yu, J. H.; Deng, Q. H.; Zhang, F. A.; Wang, G. Titanium carbide ($Ti_3C_2T_x$) MXene: A novel precursor to amphiphilic carbide-derived graphene quantum dots for fluorescent ink, light-emitting composite and bioimaging. *Carbon* **2017**, *118*, 50–57.
[38] Yoon, Y.; Lee, M.; Kim, S. K.; Bae, G.; Song, W.; Myung, S.; Lim, J.; Lee, S. S.; Zyung, T.; An, K. S. A strategy for synthesis of carbon nitride induced chemically doped 2D MXene for high-performance supercapacitor electrodes. *Adv. Energy Mater.* **2018**, *8*, 1703173.
[39] Yao, M. Y.; Chen, Y. Y.; Wang, Z.; Shao, C. M.; Dong, J.; Zhang, Q. H.; Zhang, L. L.; Zhao, X. Boosting gravimetric and volumetric energy density via engineering macroporous MXene films for supercapacitors. *Chem. Eng. J.* **2020**, *395*, 124057.
[40] Li, T. F.; Yao, L. L.; Liu, Q. L.; Gu, J. J.; Luo, R. C.; Li, J. H.; Yan, X. D.; Wang, W. Q.; Liu, P.; Chen, B. et al. Fluorine-free synthesis of high-purity $Ti_3C_2T_x$ (T = OH, O) via alkali treatment. *Angew. Chem., Int. Ed.* **2018**, *57*, 6115–6119.
[41] Zhang, T.; Matthews, K.; VahidMohammadi, A.; Han, M. K.; Gogotsi, Y. Pseudocapacitance of vanadium carbide MXenes in basic and acidic aqueous electrolytes. *ACS Energy Lett.* **2022**, *7*, 3864–3870.
[42] Feng, C.; Zhao, Z. L.; Luo, C. Y.; Wang, Y.; Wu, X. M.; Chen, W. X. Electrochemical storage mechanism of interstratification-assembled $Ti_3C_2T_x$ MXene/NiCo-LDHs electrode in alkaline, acid and neutral electrolytes. *Ceram. Int.* **2022**, *48*, 3884–3894.
[43] Sun, Q. J.; Cao, Z.; Zhang, J. L.; Cheng, H. R.; Zhang, J.; Li, Q.; Ming, H.; Liu, G.; Ming, J. Metal catalyst to construct carbon nanotubes networks on metal oxide microparticles towards designing high-performance electrode for high-voltage lithium-ion batteries. *Adv. Funct. Mater.* **2021**, *31*, 2009122.
[44] Wei, X. C.; Cai, M.; Yuan, F. L.; Lu, D.; Li, C.; Huang, H. F.; Xu, S. K.; Liang, X. Q.; Zhou, W. Z.; Guo, J. The surface functional modification of $Ti_3C_2T_x$ MXene by phosphorus doping and its application in quasi-solid state flexible supercapacitor. *Appl. Surf. Sci.* **2022**, *606*, 154817.
[45] Liu, X. L.; Lu, Z. J.; Huang, X. N.; Bai, J. F.; Li, C.; Tu, C. J.; Chen, X. X. Self-assembled S, N co-doped reduced graphene oxide/MXene aerogel for both symmetric liquid- and all-solid-state supercapacitors. *J. Power Sources* **2021**, *516*, 230682.

This is an open access article under the terms of the Creative Commons Attribution 4.0 International License (CC BY 4.0, https://creativecommons.org/licenses/by/4.0/).

© The Author(s) 2025. Published by Tsinghua University Press.